

Supplementary Information

Unraveling the Dynamic Transformation of Azobenzene-driven Redox
Electrolytes for Zn-ion Hybrid Capacitors

Ming Chen^a, Li Gong^b, Igor Zhitomirsky^c, and Kaiyuan Shi^{a*}

a) School of Materials Science and Engineering, Institute of Green
Chemistry and Molecular Engineering, Sun Yat-Sen University,
Guangzhou, Guangdong, China, 510275

b) Instrumental Analysis and Research Centre, Sun Yat-sen University,
Guangzhou, Guangdong, China, 510275

c) Department of Materials Science and Engineering, McMaster
University, Hamilton, Ontario, Canada, L8S 4L7

*Email: shiky7@mail.sysu.edu.cn

Table of Contents

- **Materials and Experimental Procedures**
- **Reversible Redox Behavior of Azobenzene Molecules**
- **In-situ Electrochemical AFM and KPFM Measurements**
- **Interfacial Characterizations of Zinc Anodes**
- **Transformative Behavior of Redox Electrolytes**
- **Electrochemical Performance of Zn//Zn Cells**
- **Electrochemical Performance of AC//Zn Cells**
- **Versatility of Azobenzene Molecules**

Materials and Experimental Procedures

1. Materials

Azobene compounds were purchased from MACKLIN. Poly(vinylidene fluoride) and activated carbon (AC) were supplied by Aladdin. The BET surface area of the AC (Product No: C299105) is $\sim 1000 \text{ m}^2 \text{ g}^{-1}$, as provided by the supplier. Zinc sulfate heptahydrate and Super-P carbon black were obtained from Alfa Aesar. All chemicals were used as received without further purification.

2. Electrolyte and cell preparation

Baseline cells were fabricated using 2 M ZnSO_4 electrolytes (Ad-Free).

Redox electrolytes were prepared by adding 0.5-5 mM azobenzene additives to 2 M ZnSO₄ solutions. Zn foils were polished with sandpaper and punched into discs for testing. The stability of metallic Zn was assessed using Zn//Zn and Zn//Ti cells. ZICs were constructed with AC cathode and Zn anode. The AC cathode was prepared by a slurry-casting method, mixing AC powder, carbon black, and poly(vinylidene fluoride) in a ratio of 8:1:1, and then coated onto stainless steel. The electrochemical performance of the cells was evaluated by assembling 2032 coin-type cells with a glass fiber separator.

3. Electrochemical analysis

The electrochemical performance of Zn//Zn and Zn//Ti cells was investigated using various electrolytes. Cyclic voltammograms (CV) were recorded using a Chenhua CHI440c potentiostat at different scan rates. Additional measurements, including chronoamperometry (CA), chronopotentiometry (CP), linear sweep voltammetry (LSV), and electrochemical impedance spectra (EIS), were conducted with a GAMRY Interface 1010E electrochemical workstation. CA measurements were performed at an overpotential of -150 mV, while CP analysis was carried out at a current density of 1 mA cm⁻². EIS data was collected over a frequency range of 0.2 Hz to 100 kHz with an alternative voltage of 5 mV. Galvanostatic charge/discharge results were obtained using a LAND CT3001A testing system, and the specific capacity of ZICs was calculated

based on the active mass of the AC cathodes.

4. Physicochemical characterization

The structural properties and molecular dimensions were analyzed using a molecular mechanics approach in combination with InDraw software. Molecular accessible area and solvent-excluded volume were determined using Connolly's program^{1, 2}. The log P was computed to evaluate the molecule's hydrophobicity³. The energy levels of the lowest unoccupied molecular orbital (LUMO) and the highest occupied molecular orbital (HOMO) were estimated using the molecular orbital package. The morphology of cycled electrodes was examined using a Quanta 400FEG scanning electron microscope (SEM). Structural analysis was conducted using X-ray diffraction (XRD) with a Rigaku D/max 2200 diffractometer. Interphase compositions were analyzed *via* Time-of-Flight Secondary Ion Mass Spectrometry (TOF-SIMS) using a TOF.SIMS5–100 system. The chemical states on the surface and after deep sectioning were examined using X-ray photoelectron spectroscopy (XPS) with an ESCALAB 250Xi (Thermo Fisher) instrument. *In-situ* EC-AFM tests were performed on a custom Bruker Dimension FastScan platform with an RTESPA-150 probe, utilizing PeakForce Tapping techniques to investigate morphology evolution and quantitative mechanical properties. Surface topography and contact potential distribution were examined by Kelvin Probe Force Microscopy (KPFM) with a metal-coated electrostatic probe. UV–vis

spectroelectrochemical measurements were conducted with a Cary 6000i spectrophotometer and a mini-electrochemical cell with ITO-coated glass as the working electrode and a Pt wire as the counter electrode.

Supplementary Note 1: Reversible Redox Behavior of Azobenzene Molecules

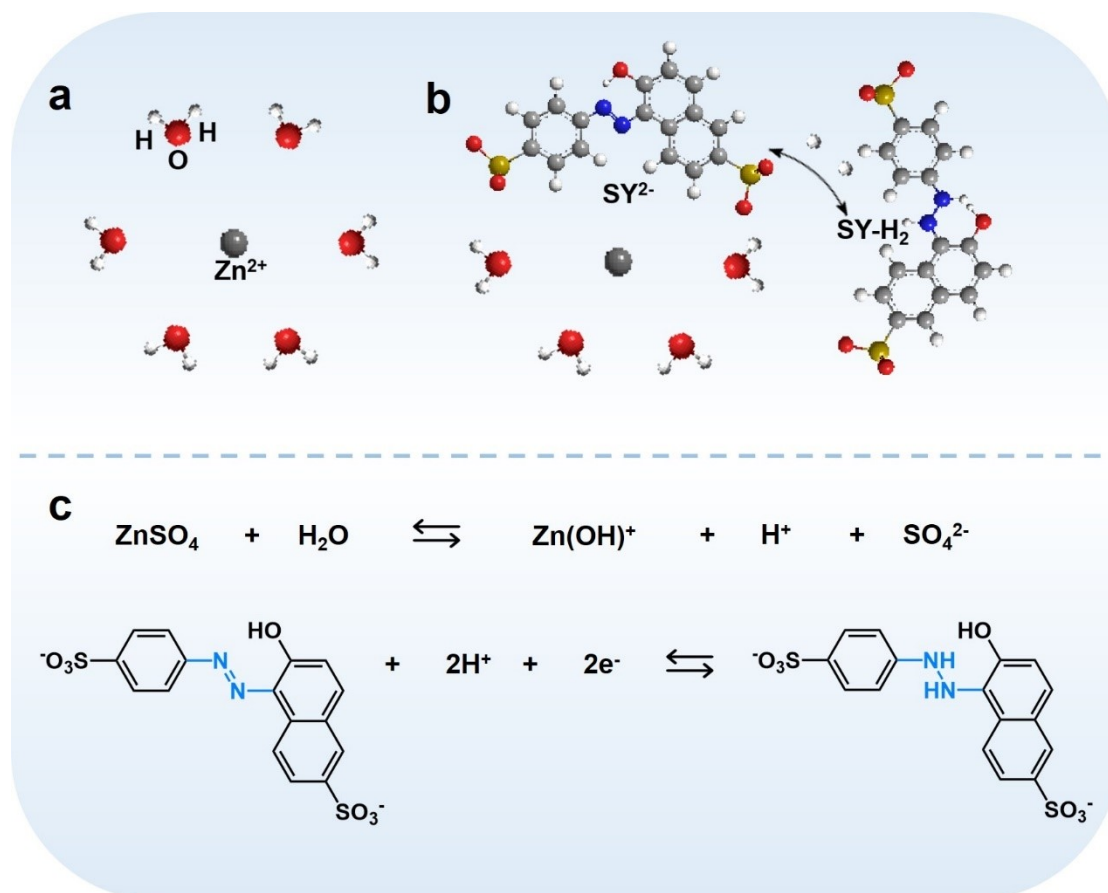


Figure S1 Proposed Zn²⁺ solvation structure in ZnSO₄-based electrolytes, (a) with and (b) without SY additives. (c) Hydrolysis of zinc Sulfate and corresponding reversible redox behavior of Sunset Yellow (SY) molecules based on the analysis.

In ZnSO₄-based electrolytes, Zn²⁺ cations engage in electrostatic interactions with water molecules as they undergo solvation, resulting in the formation of a hydration shell around the cations (Figure S1a). The shell consists of densely packed water molecules attracted to the positively charged Zn²⁺.^{4, 5} In contrast, anionic additives orient themselves towards

Zn^{2+} cations due to the electrostatic attraction (Figure S1b). The polar functional group of SY molecules reduces interactions between Zn^{2+} and H_2O by substituting adjacent water, while their conjugated structure enhances proton transfer and rearranges the solvation environment^{6, 7}.

The hydrolysis of zinc sulfate leads to the formation of zinc hydroxide, contributing to the acid-base behavior of the electrolyte (Figure S1c). Hydrolyzed Zn^{2+} cations, surrounded by a dense shell of water molecules, establish a proton-conducting network through the Grotthuss mechanism^{4, 8}. The network facilitates rapid H^+ transfer by the sequential hopping of protons between adjacent H_2O *via* hydrogen bonds. Furthermore, zinc hydroxide compounds can form a protective passivation layer that inhibits parasitic reactions, while proton transfer generates acids and bases^{9, 10}. It has been demonstrated that the hydrogen-bonded network is vital for the mass transport of protons through H^+ diffusion and migration^{11, 12}.

The protonation behavior of SY molecules involves electron transfer and protonation reactions, leading to the formation of $\text{SY}^{2-}/\text{SY-H}_2$ redox couples^{13, 14}. As a result, incorporating SY molecules enhances proton and electron transfer dynamics within ZnSO_4 -based electrolytes. Modification of solvation behavior underscores the potential of azobenzene-driven redox electrolytes to facilitate proton conduction and enhance the electrochemical performance of ZICs.

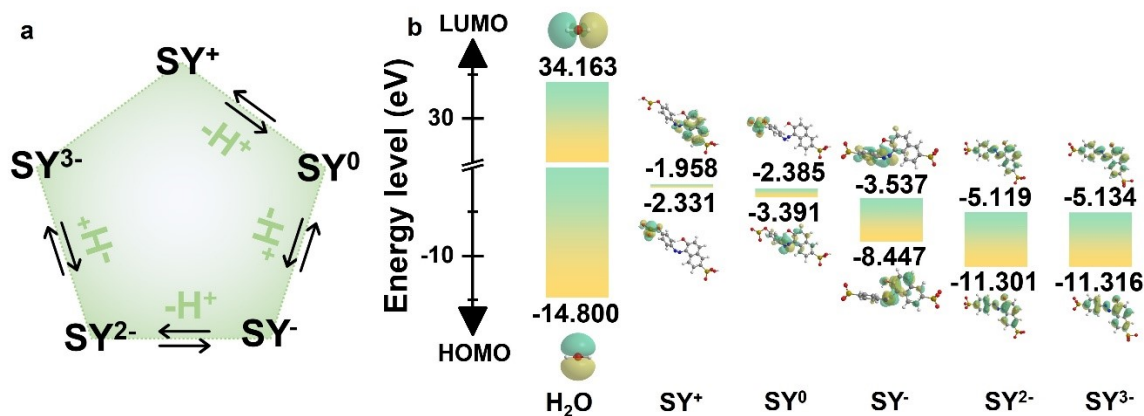


Figure S2 a) Protonation and electron transfer processes of SY-derived species. b) Calculations of LUMO/HOMO energy levels and the orbital energy gap ($\Delta E = E_{\text{LUMO}} - E_{\text{HOMO}}$) of the H₂O, SY⁺, SY⁰, SY⁻, SY²⁻ and SY³⁻ molecules. The green clusters represent positive regions, while the yellow spots as negative regions.

The reversible structural transformation of the SY molecule, along with its allotropic transition, highlights its potential for charge storage. Figure S2a illustrates the transformation of SY-derived species during the protonation processes, where the molecules undergo electron transfer reactions that are essential for forming different oxidation states, including SY⁺, SY⁰, SY⁻, SY²⁻, and SY³⁻. The transition between different protonated and deprotonated forms highlights the reversibility of SY-containing electrolytes in electrochemical processes. Furthermore, the structural adaptability of SY molecules enhances their charge transfer behavior within the electrolyte matrix. It has been shown that the redox-active molecules enhance the dynamic ion and charge transport of electrolytes across the solid-liquid interface^{15, 16} In addition, incorporating azobenzene

anions as electrolyte additives inhibits the aggregation of Zn^{2+} cations while promoting efficient electron flow.

As shown in Figure S2b, the various protonation states of the SY molecule are analyzed based on the lowest unoccupied molecular orbital (LUMO) and highest occupied molecular orbital (HOMO). The HOMO energy level reflects the electron-donating capacity of the molecules and identifies potential nucleophilic sites. On the other hand, the LUMO energy level indicates the electron acceptance capacity, facilitating the attraction of electrophilic species¹⁷⁻²⁰. The results reveal the energy gap ($\Delta E = E_{\text{LUMO}} - E_{\text{HOMO}}$) narrows progressively as the molecule undergoes deprotonation, indicating an increased tendency for electron transfer between SY^+ with SY^{3-} . It is worth noting that the computed ΔE of SY^+ , SY^0 , SY^- , SY^{2-} , and SY^{3-} is lower than that of the H_2O , which helps inhibit electrolyte electrolysis during electrochemical cycling²¹.

The visualization of molecular orbitals provides insight into the arrangement of electrons within the molecule across different protonation states. As the molecule transitions through these states, the distribution of electrons shifts, reflecting changes in electron localization during redox transformations. It is important to note that SY-derived species undergo the allotropic transformation over the electrochemical reaction. As a result, the HOMO/LUMO energy levels of the molecules could vary due to the conformational effect²². It has been shown that as the HOMO energy levels

increase, the binding properties between molecules and metal surfaces are strengthened²³. In addition, the lower LUMO energy level of SY²⁻/SY³⁻ indicates an enhanced interaction between the electrolyte and Zn anode²⁴,²⁵, resulting from the donation of electrons from the HOMO energy level. The examination of energy levels highlights the importance of protonation behavior in the electrochemical behavior of SY-containing electrolytes. It is proposed that fluctuations in local pH within the aqueous electrolyte enhance the charge transfer process of azobenzene molecules. This behavior is thoroughly examined in Figure S21, focusing on tautomeric and acid-base neutralization processes.

Supplementary Note 2: *In-situ* Electrochemical AFM and KPFM Measurements

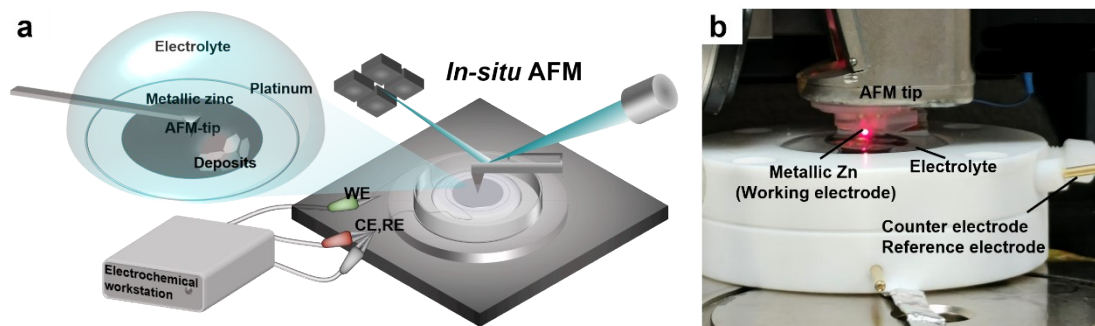


Figure S3 (a) Scheme of the in-situ electrochemical AFM testing device for analyzing Zn^{2+} plating with different electrolytes and (b) corresponding experimental photograph.

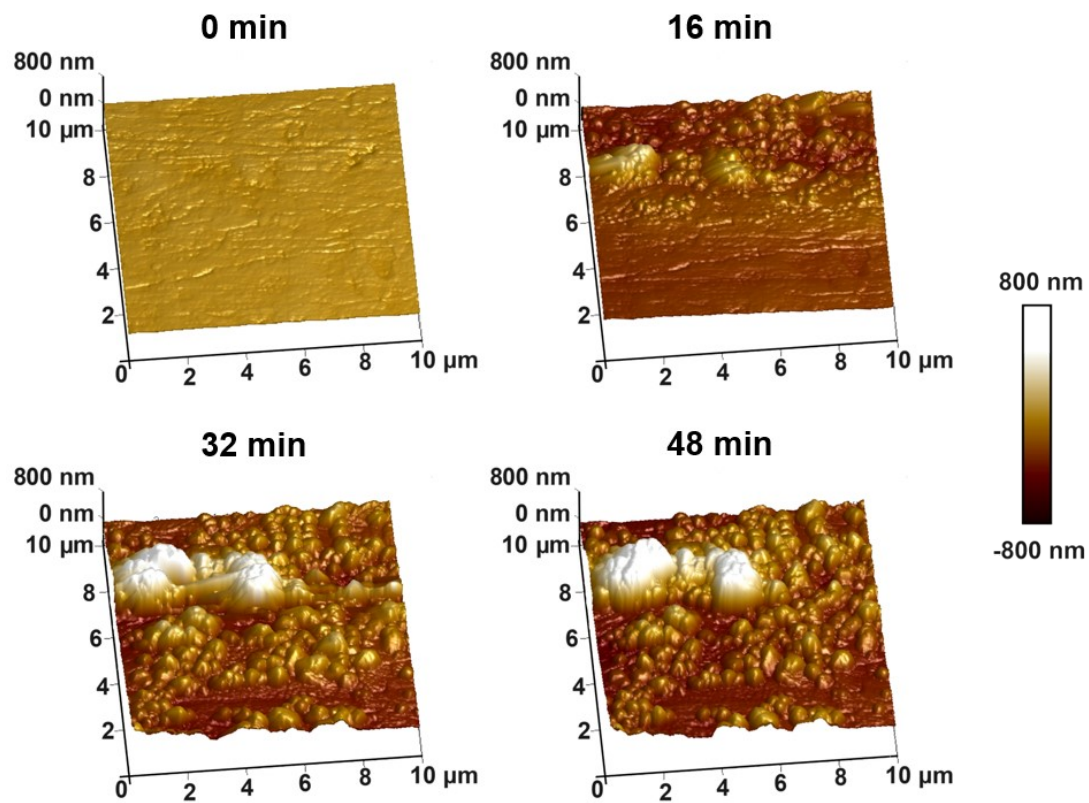


Figure S4 3D topography evolution of Zn deposits prepared with the Ad-Free electrolyte as plating time increases. The deposition was carried out under *in-situ* electrochemical AFM conditions at a current of 1.0 mA cm^{-2} .

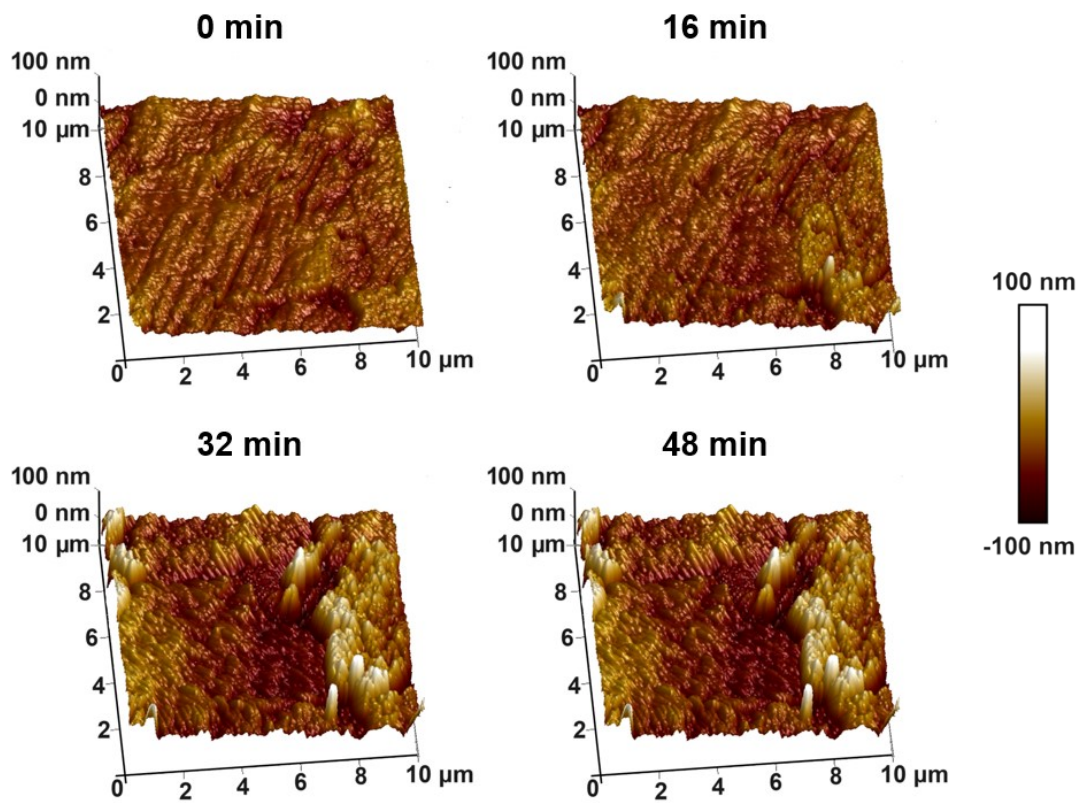


Figure S5 3D topography evolution of Zn deposits prepared with the SY-containing electrolyte as plating time increases. The deposition was carried out under *in-situ* electrochemical AFM conditions at a current of 1.0 mA cm^{-2} .

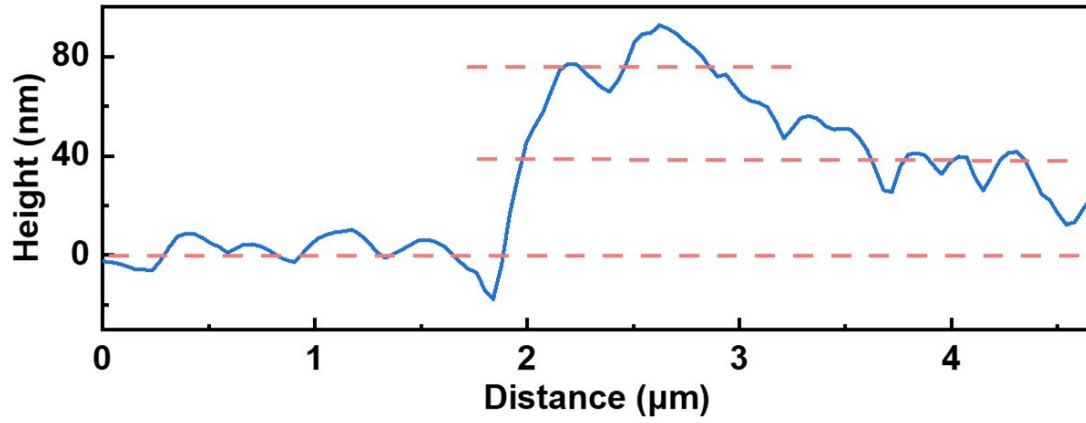


Figure S6 Variation in height versus distance of Zn deposits, prepared by SY-containing electrolyte, as indicated by the blue dashed line in Figure 2d (Right).

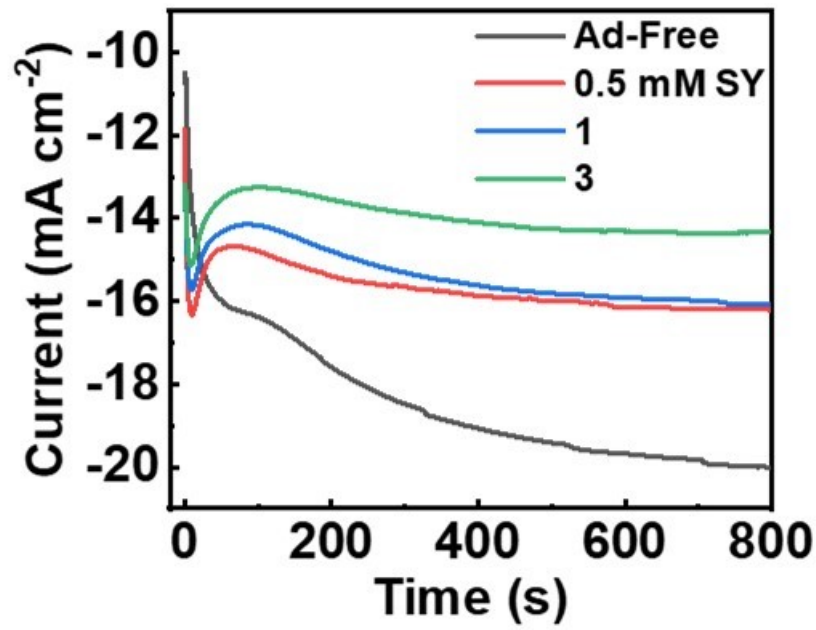


Figure S7 Chronoamperometric curves of Zn²⁺ plating using ZnSO₄-based electrolytes with increasing amounts of SY additives at an overpotential of -150 mV.

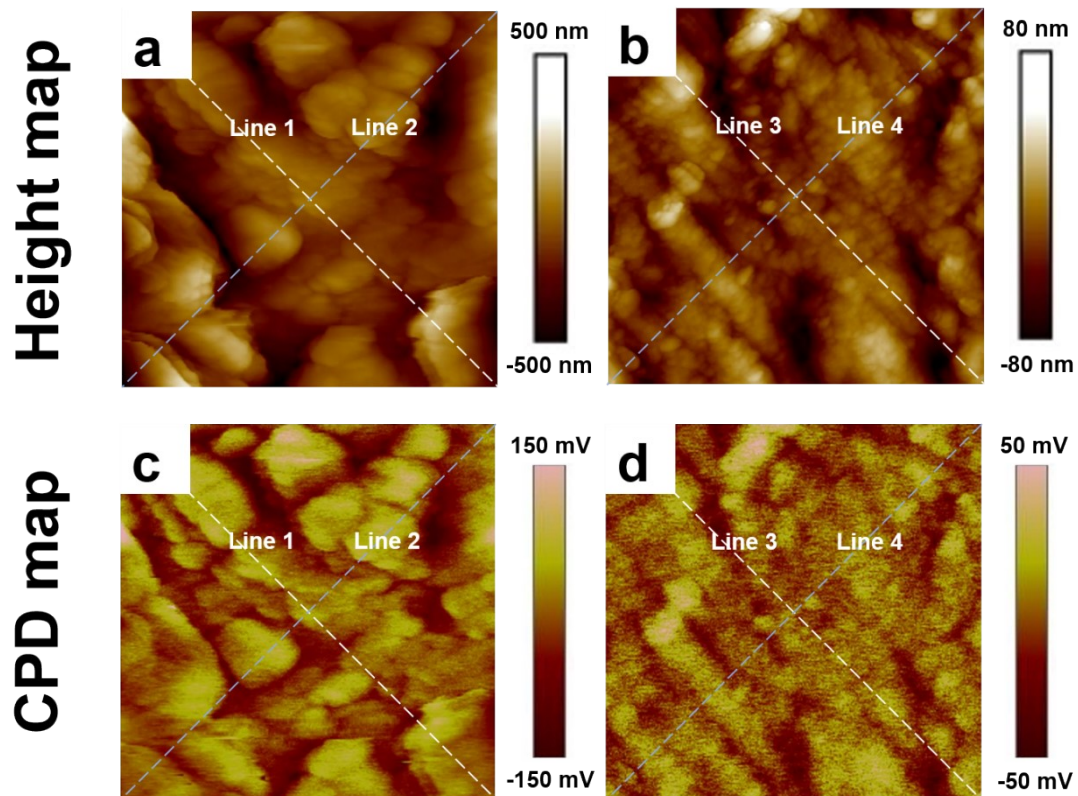


Figure S8 KPFM analysis of (a and b) surface topography and (c and d) potential distribution of Zn deposits, prepared by (a and c) Ad-Free and (b and d) SY-containing electrolytes after 10 cycles at 2 mA cm^{-2} and 1 mAh cm^{-2} in Zn//Zn cells.

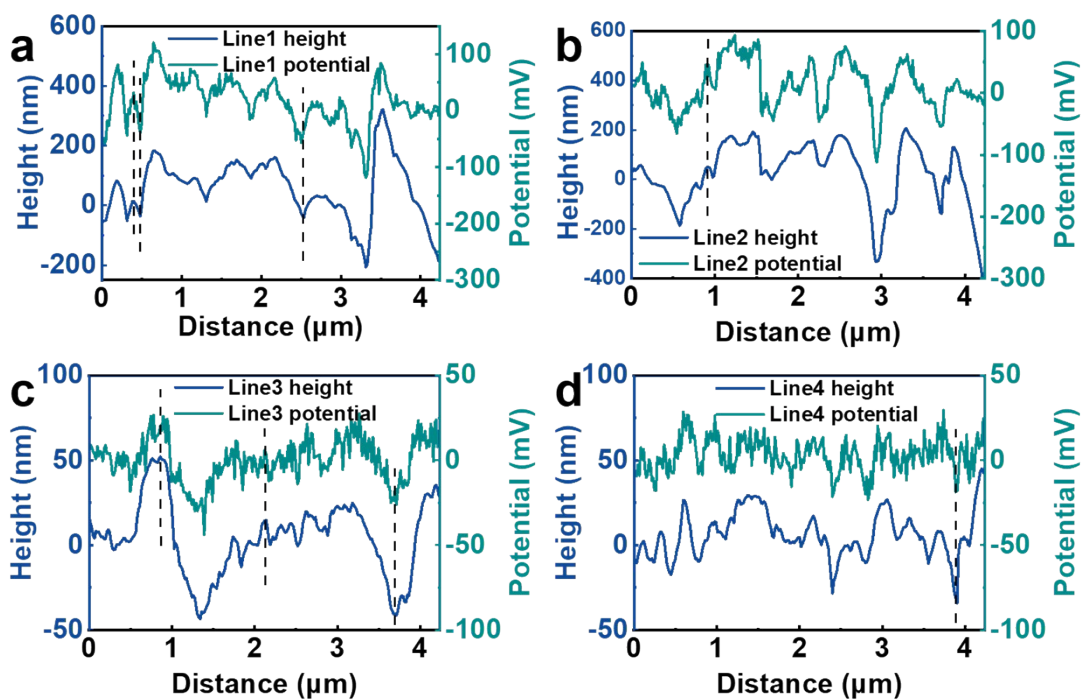


Figure S9 Surface height and corresponding potential, measured by KPFM analysis, of Zn deposits prepared by the (a and b) Ad-Free and (c and d) SY-containing electrolyte. The data were collected from the dashed cross-lines indicated in Figure S8.

Table S1 Heights (H) and corresponding potentials (V) obtained from the KPFM analysis presented in Figure S9.

	Ad-Free electrolyte		SY-containing electrolyte	
H_{\max} (nm)	13.79	50.11	14.90	52.30
V_{\max} (mV)	31.99	45.29	6.14	26.10
H_{\min} (nm)	-36.41	-40.58	-34.16	-41.38
V_{\min} (mV)	-39.03	-56.73	-18.52	-25.94

The data illustrates the surface potential at varying heights for different electrolytes, obtained from KPFM measurements as shown in Figures S8 and S9. The results indicate that the topographical environment influences electrostatic interactions. For the Ad-Free electrolyte, the maximum height (H_{\max}) is recorded at 13.79 nm with a corresponding potential (V_{\max}) of 31.99 mV, while the SY-containing electrolyte shows a higher H_{\max} of 14.90 nm and a V_{\max} of 6.14 mV. It is demonstrated that while the Ad-Free electrolyte generates greater height differences and potential variation, the SY-containing electrolyte offers a more stable electrostatic environment. The uniform distribution of surface potential, based on the SY-containing electrolyte, reduces the reaction rate of Zn^{2+} deposition, thus enhancing the electrochemical stability of the cells. Overall, the KPFM analysis provides evidence of the electrostatic behavior of the passivated interphase.

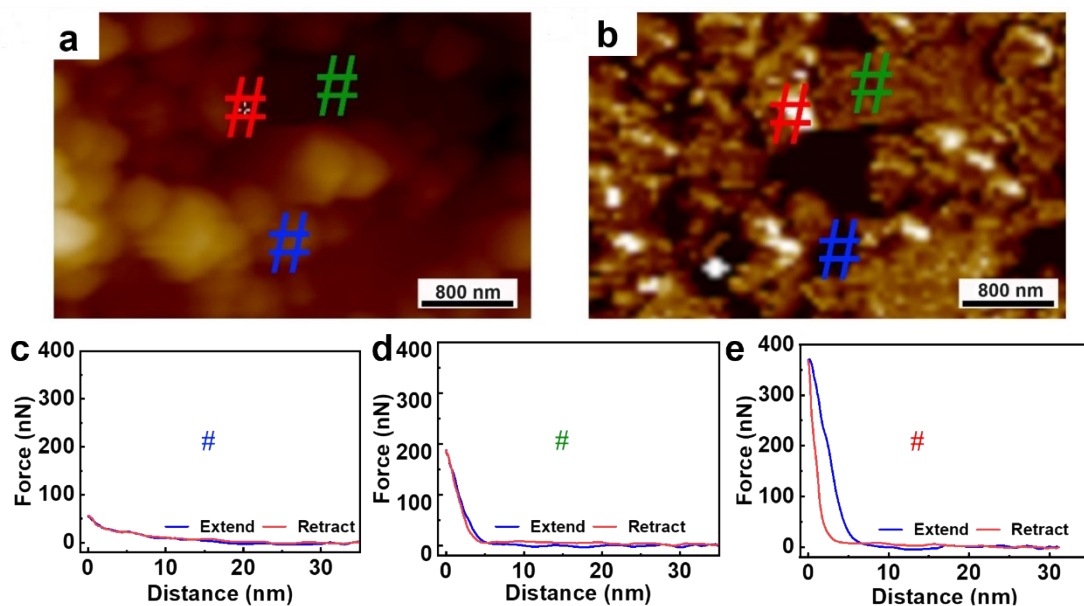


Figure S10 (a) Surface topography, (b) DMT modulus, and (c-d) the corresponding force-displacement curves of Zn deposits, obtained from the Ad-Free electrolyte using *in-situ* EC-AFM at 1.0 mA cm^{-2} after 16 min of plating. The force-displacement curves of the #” points were presented in (c) blue, (d) green, and (e) red, respectively.

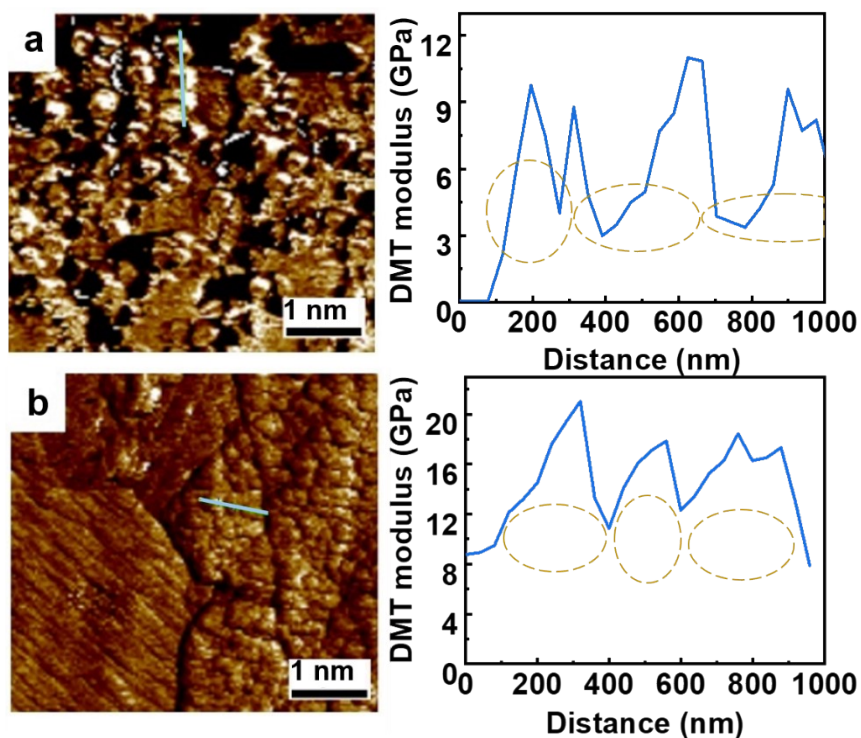


Figure S11 DMT modulus mapping and modulus variation of Zn deposits, obtained from the (a) Ad-Free and (b) SY-containing electrolyte using *in-situ* EC-AFM at 1.0 mA cm^{-2} after 32 min of plating. The change in modulus (left) is measured across the blue line indicated in the mapping results (right).

Measurements of the DMT modulus revealed distinct behaviors in Zn deposits prepared with different electrolytes. Analysis of the intragrain and intergrain DMT modulus indicates that the Ad-Free electrolyte produces Zn deposits with large non-uniformity (Figure S11a). The presence of brittle inorganic by-products is reflected in the pronounced modulus variations along the blue line. In contrast, the SY-containing electrolyte yields a more homogeneous structure, with reduced modulus fluctuations that lead to a stable and cohesive deposit (Figure S11b).

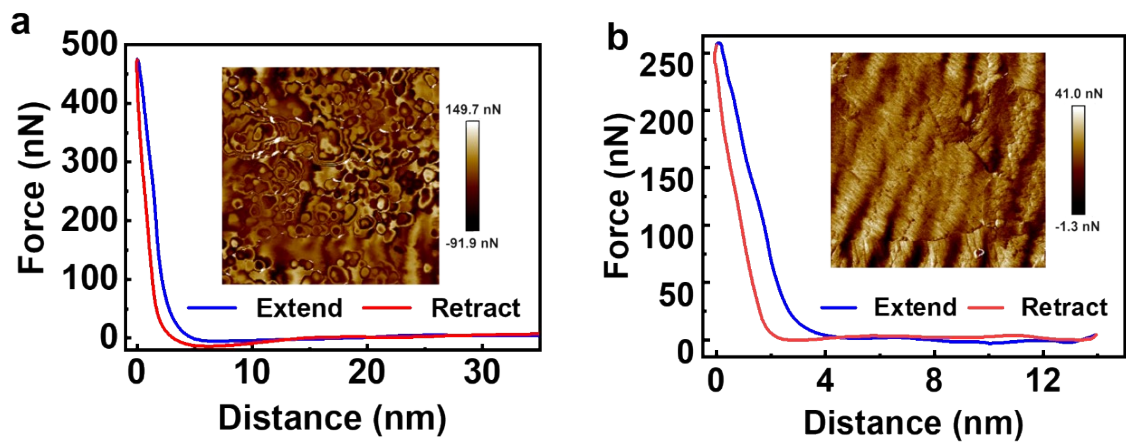


Figure S12 Typical force-displacement curves and corresponding adhesion mapping (Inset) of Zn deposits, obtained from the (a) Ad-Free and (b) SY-containing electrolyte using *in-situ* EC-AFM at 1.0 mA cm^{-2} after 48 mins of plating.

Supplementary Note 3: Interfacial Characterizations of Zinc Anodes

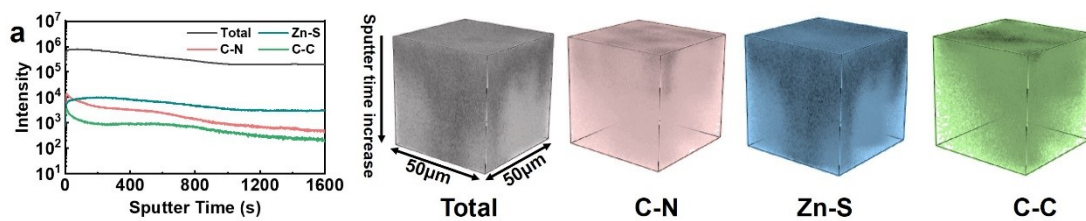


Figure S13 TOF-SIMS depth profiling (Left) and corresponding 3D composition of the electrodes in the Ad-Free electrolyte at 2 mA cm^{-2} and 1 mAh cm^{-2} after 200 cycles.

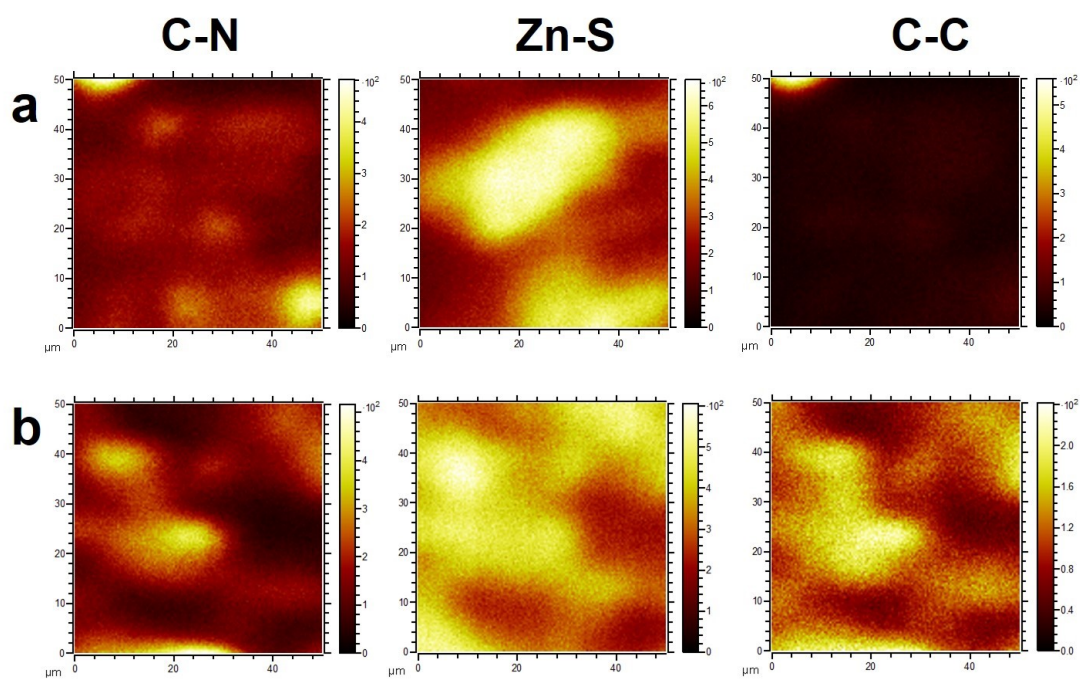


Figure S14 TOF-SIMS 2D composition of the electrodes tested at 2 mA cm^{-2} and 1 mAh cm^{-2} after 200 cycles, using the (a) Ad-Free and (b) SY-containing electrolyte.

Table S2 Atomic percentage of each element derived from the XPS survey spectra of cycled electrodes in different electrolytes.

Components Electrolyte	Zn2p	C1s	O1s	S2p	N1s
Ad-Free	24.7138	23.2843	49.1267	2.04485	0.8303
SY-containing	21.6395	21.4733	49.5988	6.34617	0.9427

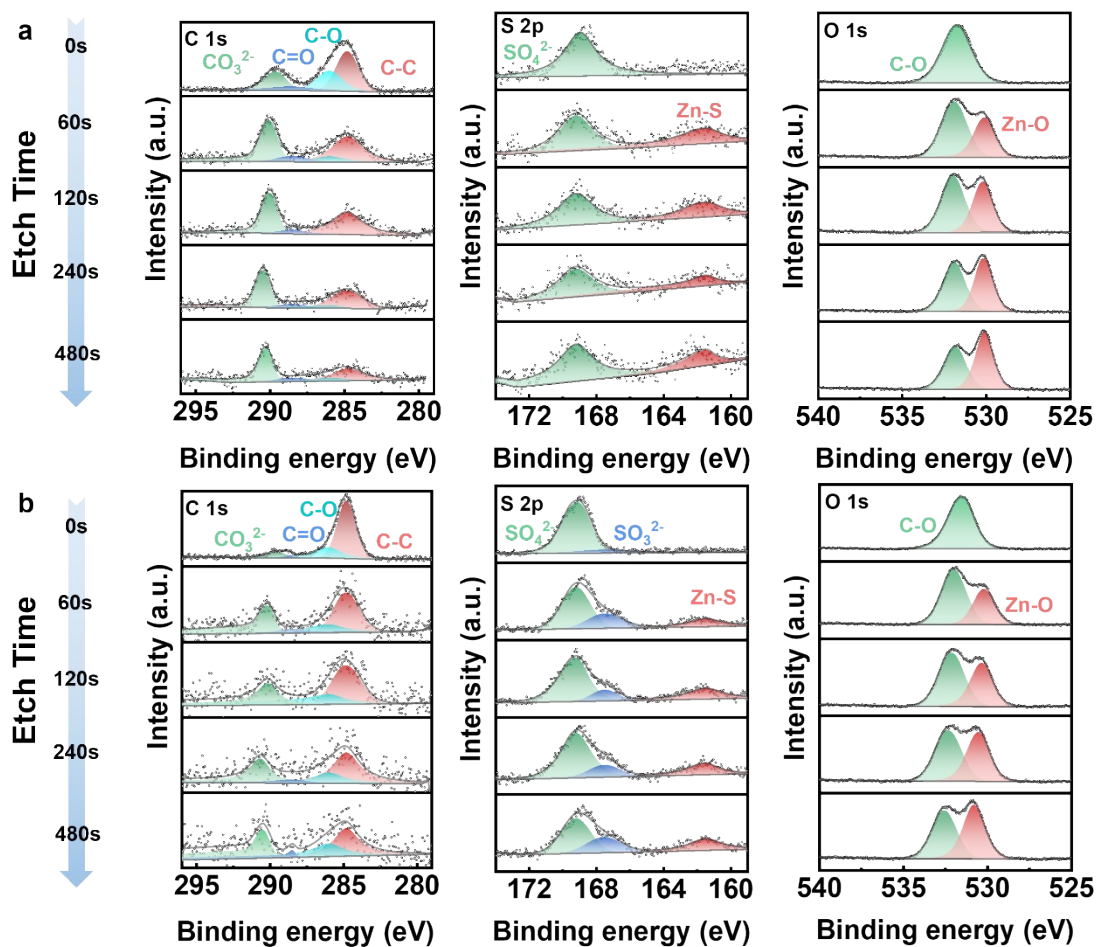


Figure S15 XPS depth profile with increased etching time for C 1s, S 2p, and O 1s of the electrodes obtained from Zn//Zn cells at 2 mA cm^{-2} and 1 mAh cm^{-2} after 200 cycles, using the (a) Ad-Free and (b) SY-containing electrolytes.

Table S3 The proportion of surface organic and inorganic components

Electrolyte Etch Time	Ad-Free		SY-containing	
	Inorganics	Organics	Inorganics	Organics
0s	20.00%	80.00%	7.84%	92.16%
60s	44.12%	55.88%	36.06%	63.94%
120s	42.51%	57.49%	30.79%	69.21%
240s	38.74%	61.26%	31.85%	68.15%
480s	45.99%	54.01%	32.13%	67.87%

calculated from C 1s peak spectrum as shown in Figure S15.

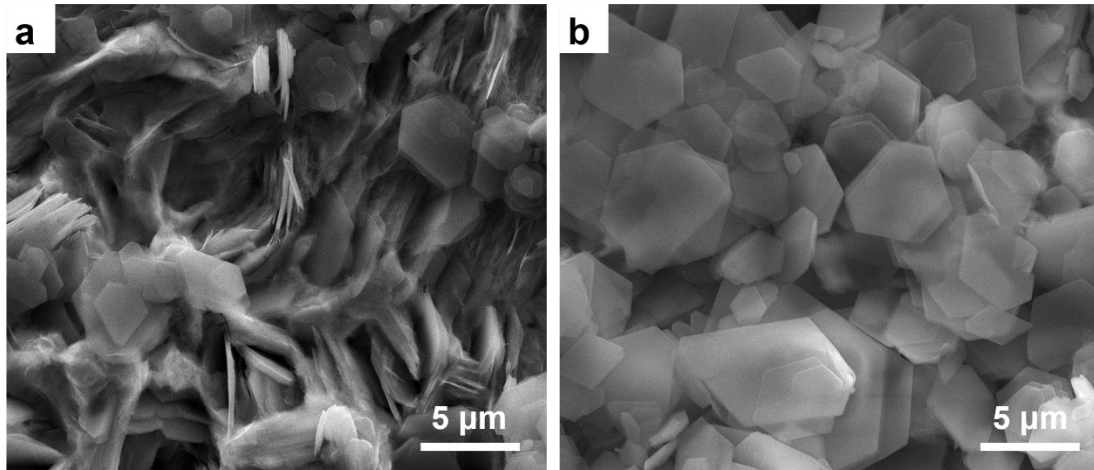


Figure S16 SEM images of Zn electrodes obtained from Zn//Zn cells at 2 mA cm⁻² and 1 mAh cm⁻² after 200 cycles, using the (a) Ad-Free and (b) SY-containing electrolytes.

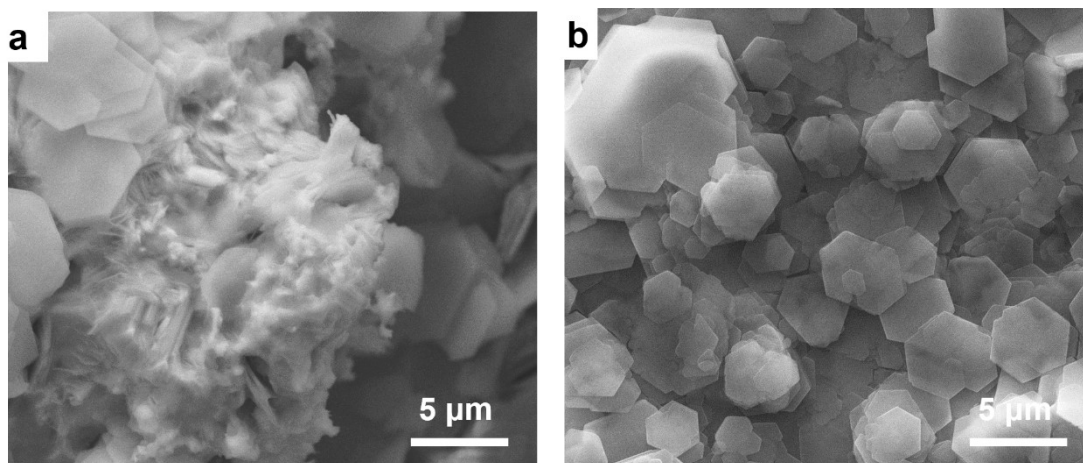


Figure S17 SEM images of Ti electrodes obtained from Zn//Ti cells at 2 mA cm^{-2} and 1 mAh cm^{-2} after 200 cycles, using the (a) Ad-Free and (b) SY-containing electrolytes.

SEM images reveal the morphological differences in Ti electrodes after cycling with Zn//Ti cells. The use of the Ad-Free electrolyte leads to the formation of Zn dendrites on the Ti electrode, attributed to uneven Zn ion deposition (Figure S17a). These dendrites penetrated the separator, causing irregular deposition patterns that resulted in short circuits over extended cycles. In contrast, the SY-containing electrolyte effectively inhibits dendrite formation, resulting in a smoother and more uniform deposition on the Ti electrode (Figure S17b).

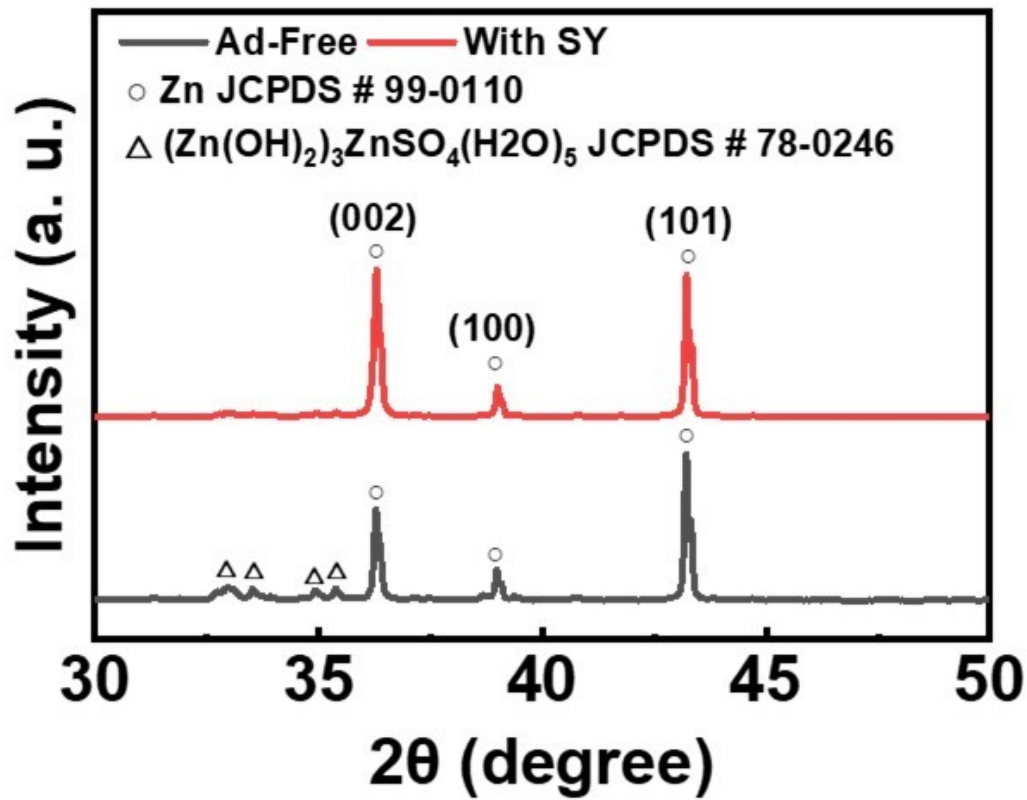


Figure S18 XRD results of Zn electrodes obtained from Zn//Zn cells with different electrolytes, tested at 2 mA cm^{-2} and 1 mAh cm^{-2} after 200 cycles.

Supplementary Note 4: Transformative Behavior of Redox Electrolytes

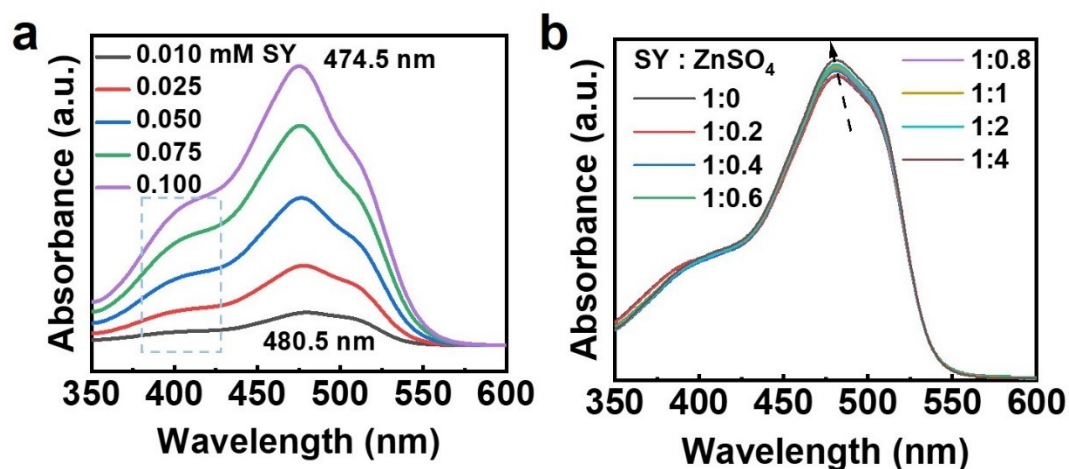


Figure S19 UV-vis spectroscopic analysis of a) ZnSO₄-based electrolytes with increased amounts of SY additives and b) the solutions with different SY: ZnSO₄ ratios.

The UV-vis absorption spectra reveal the ionic coordination of azobenzene-driven redox electrolytes. A distinct double-headed band in the 375–425 nm range is triggered by an allotropic transformation of SY molecules (Figure S19a). Increasing the amounts of SY leads to rearrangements in the molecular structure of the complexes, resulting in changes in electron distribution and spatial geometry. These transformations may be induced by ionic interactions within the ZnSO₄-based electrolytes²⁶, which yield distinctive spectral characteristics. Furthermore, the observed hypsochromic change in the $n\text{-}\pi^*$ transition within the 470–490 nm range is attributed to the chelation coordination interaction between SY molecules and Zn²⁺ cations²⁷. The variation in the SY: ZnSO₄ ratios results in a blue shift of the $n\text{-}\pi^*$ transition (Figure S19b).

This change indicates that the electronic properties of SY molecules could be altered due to coordination bonding with Zn^{2+} , thus leading to changes in the energy levels of molecular orbitals^{28, 29}. The shift to shorter wavelengths suggests that the binding properties with Zn^{2+} ions stabilize the molecule. The colorimetric responses of dye solutions with different cations are applied in the design of metal ion detection³⁰. Moreover, the chelation interaction provided by SY molecules reduces Zn^{2+} aggregation, thereby impeding dendrite growth during the plating process. Overall, the UV-vis results indicate that the coordination dynamics between SY molecules and metal ions influence the electronic properties and structural behavior of azobenzene-driven redox electrolytes.

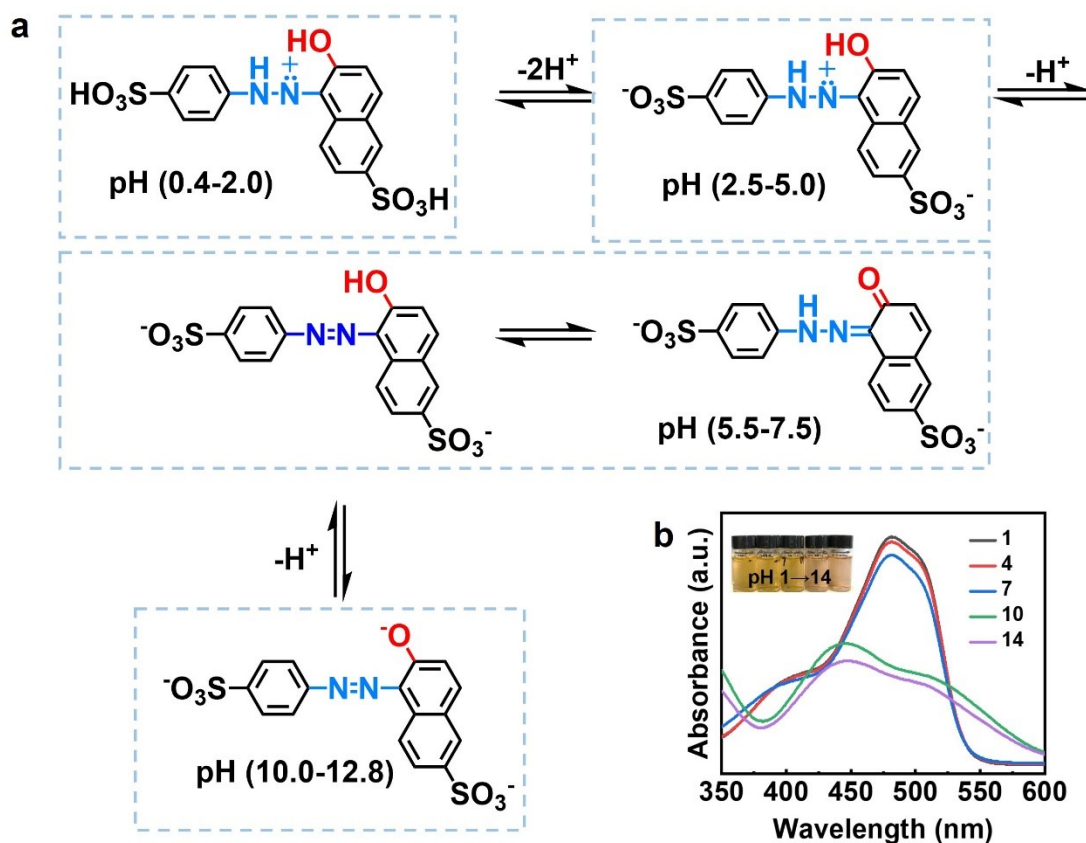


Figure S20 a) Tautomeric and acid-based equilibrium for SY molecules and b) UV-vis spectroscopic analysis of SY aqueous solutions at varying pH values (Inset: color changes from orange to pink).

The reversible charge transfer of azobenzene compounds is accompanied by their structural transformations in aqueous electrolytes³¹. The structural changes of SY molecules involve both tautomeric shifts and acid-base equilibria, which are highly dependent on pH conditions^{32, 33}. The transformations occur under varying conditions, as illustrated in the scheme (Figure S20).

1. Acidic Conditions (pH<2.0): In a strongly acidic environment, the protonated form of SY molecules, SY⁺, predominates. This form results

from the protonation of the azo nitrogen ($-\text{N}=\text{N}-$). As the pH increases above 2.0, the molecule undergoes deprotonation, transforming into various anionic forms.

2. Transition in pH 2.0 to 5.0 Range: As the pH rises above 2.0, SY molecules progressively deprotonate, leading to the formation of its mono-, di-, and tri-anionic species (SY^- , SY^{2-} , and SY^{3-}). These structural changes correspond to a gradual loss of protons from the molecule, accompanied by charge transfer.
3. Neutral to Slightly Alkaline Conditions (pH 5.5–7.5): In this pH range, the molecules exist predominantly in their di-anionic form (SY^{2-}), which exhibits tautomeric shifts. The equilibrium between these tautomers is highly sensitive to changes in pH, causing a dynamic shift in the molecular structure.
4. Strongly Alkaline Conditions (pH>10.6): In strongly alkaline environments, the di-anionic form SY^{2-} further deprotonates to form the tri-anion (SY^{3-}), representing the fully deprotonated state of the molecule. This structural transformation reflects the final stage of deprotonation.

The hydrolysis of zinc sulfate plays a crucial role in determining the acid-base behavior of the electrolyte. During the electrochemical process, the application of voltage can trigger water electrolysis, resulting in the generation of hydroxyl ions (OH^-) at the cathode and protons (H^+) at the

anode. This accumulation of H^+ decreases the local pH, intensifying acidic conditions around the metallic Zn. These acidic conditions, in conjunction with the electric field, enhance the reduction of SY^{3-} to SY^{2-} derivatives, thus promoting interfacial charge transfer. Simultaneously, the multi-anionic species undergo oxidation to their deprotonated forms through the -OH and -NH-NH- groups. The proton dissociation behavior of the molecules reflects the stepwise deprotonation processes, with each pH-dependent transformation resulting in a distinct structural form. The dynamic nature of structural variations is essential for charge transfer, facilitated by the hydrogen-bonded network in the aqueous environment. Furthermore, electrophoretic behavior drives the migration and transport of ionic molecules, promoting interfacial redox reactions. The structural changes of azobenzene compounds highlight their adaptability as redox-active molecules to varying pH levels, which influences the stability and electrochemical properties. It is noteworthy that tautomeric and acid-base neutralization processes enable proton (charge) transfer without involving electrons. The electron transfer of azobenzene molecules exhibits pH dependence, with natural/mild alkaline conditions being favorable for both charge and electron transfer²⁸. The responsiveness over electrochemical cycling enhances electron transfer processes at the double-layer interface, thereby improving the capacity of ZICs.

Supplementary Note 5: Electrochemical Performance of Zn//Zn Cells

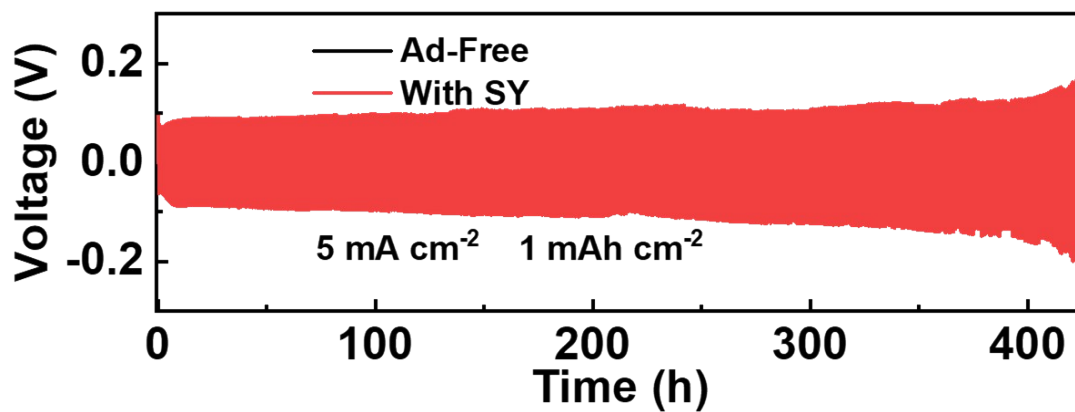


Figure S21 Cycling behavior of Zn//Zn cells at 5 mA cm⁻² and 1 mAh cm⁻² in the Ad-Free and SY-containing electrolytes.

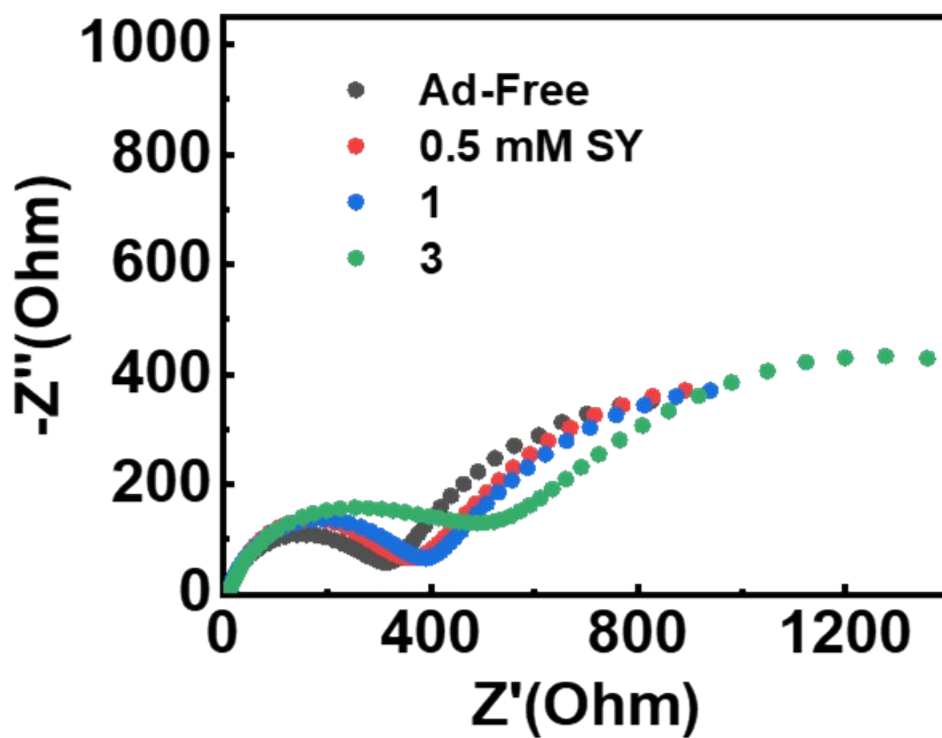


Figure S22 EIS spectra of Zn//Zn cells, prepared by ZnSO₄-based electrolytes with increasing amounts of SY additives.

Supplementary Note 6: Electrochemical Performance of AC//Zn Cells

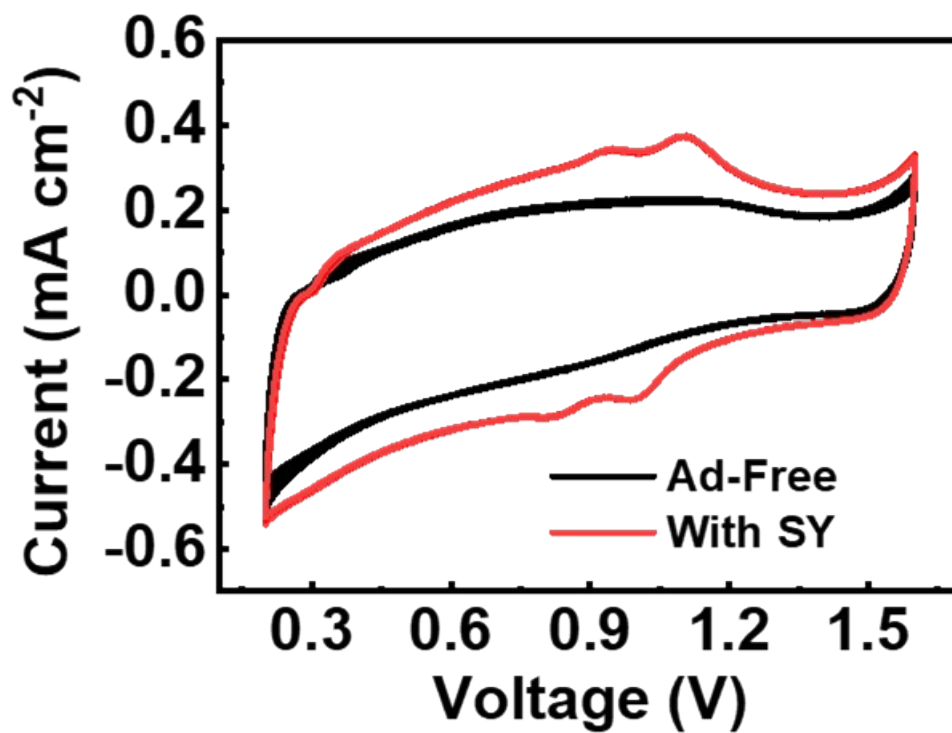


Figure S23 CV profiles for the first 5 cycles at a scan rate of 1.0 mV s⁻¹ for the ZICs, prepared by the Ad-Free and SY-containing electrolytes.

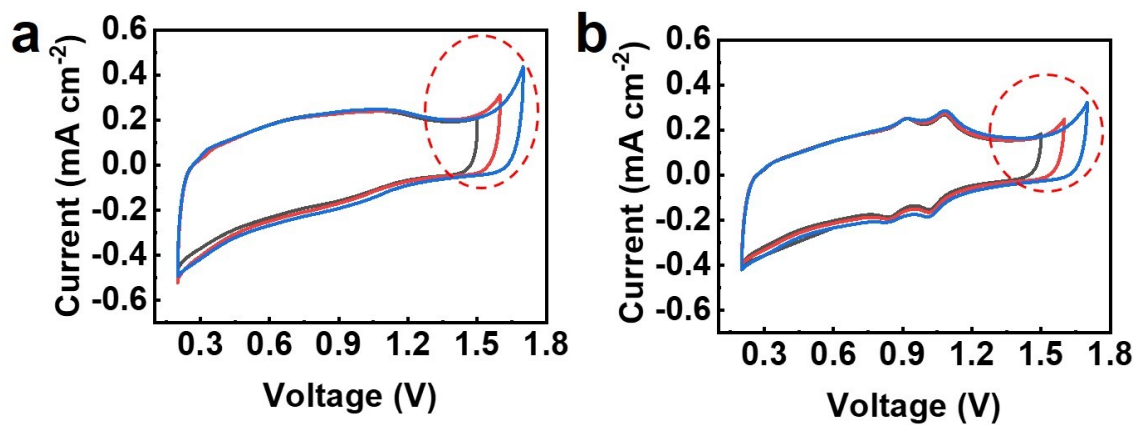


Figure S24 CV profiles in different voltage windows at a scan rate of 1.0 mV s^{-1} of the ZICs, prepared by the (a) Ad-Free and (b) SY-containing electrolytes.

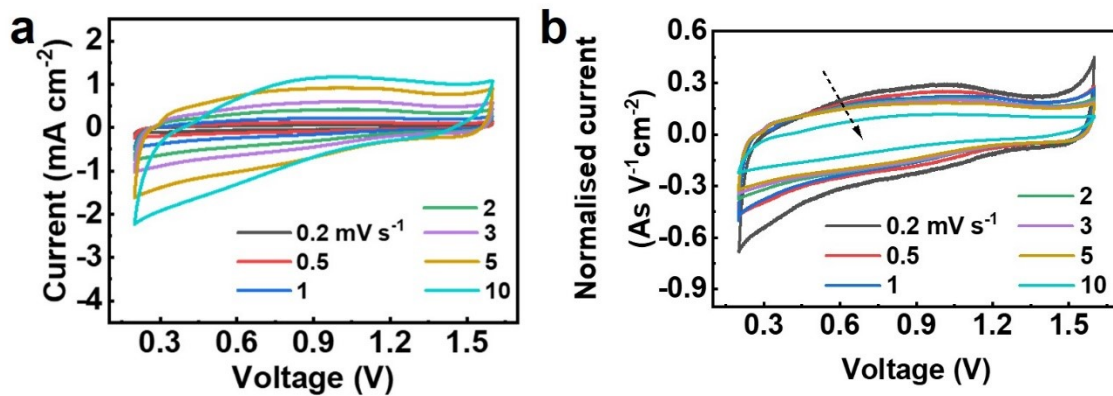


Figure S25 CV profiles of the ZIC prepared with the Ad-Free electrolyte:
a) at various scan rates and b) normalized by scan rates.

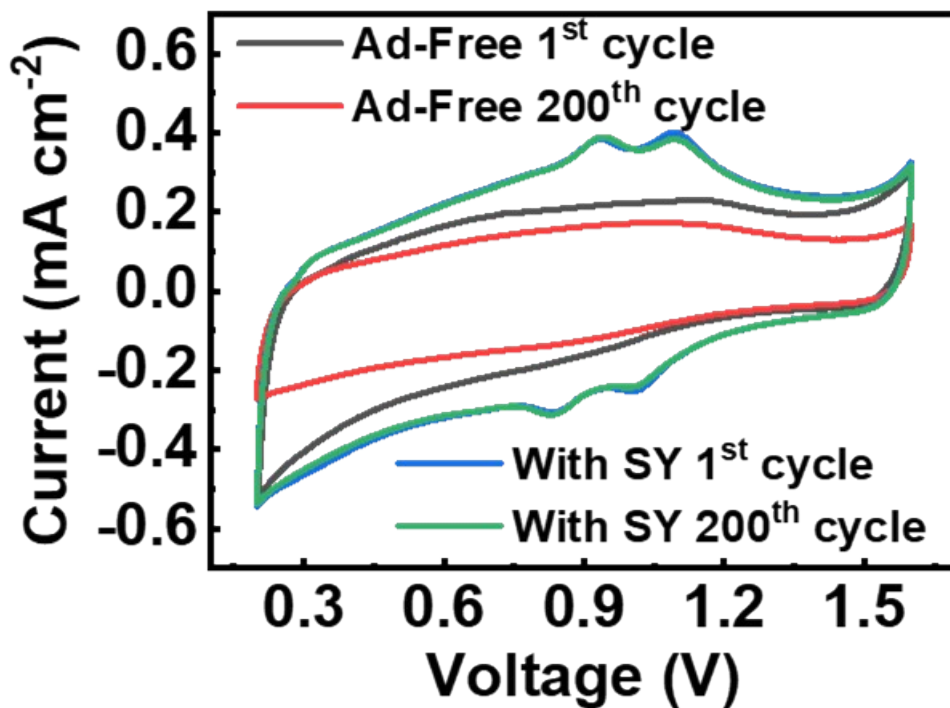


Figure S26 CV profiles before and after 200 cycles at a scan rate of 1.0 mV s⁻¹ for the ZICs, prepared by the Ad-Free and SY-containing electrolytes.

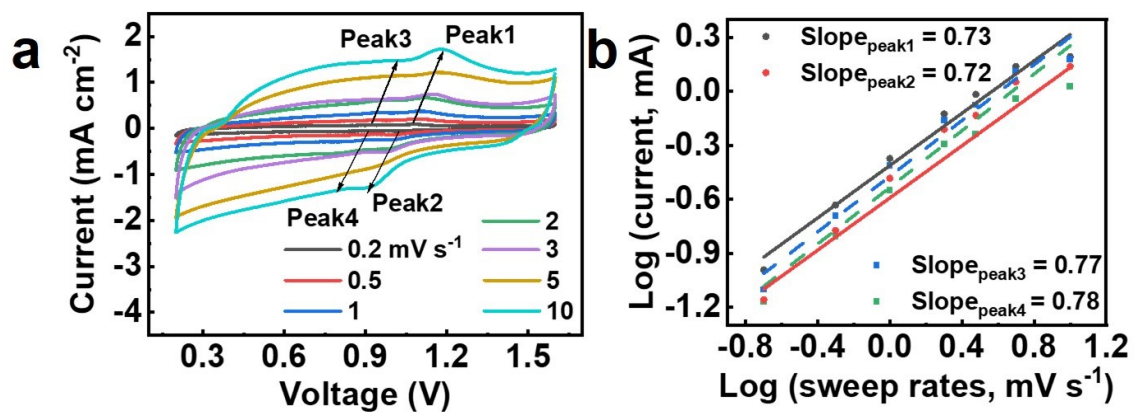


Figure S27 (a) CV profiles at various scanning rates of the ZIC, prepared by the SY-containing (3 mM) electrolyte. (b and c) Corresponding peak slopes determined by line-fitting $\log(i)$ – $\log(v)$ plots from the CV data.

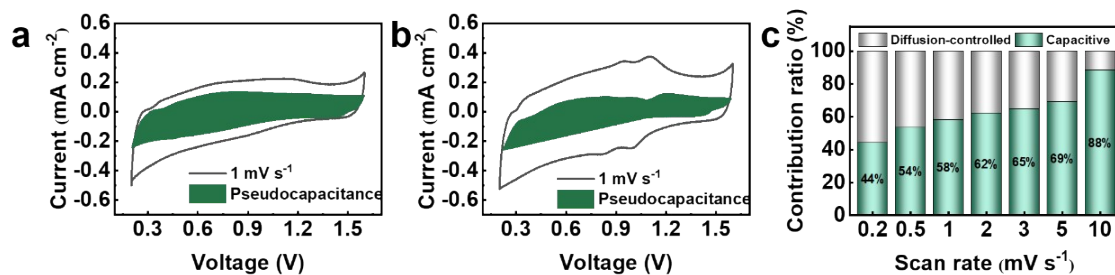


Figure S28 (a and b) Separation of the capacitive and diffusion-controlled contributions at a scan rate of 1.0 mV s^{-1} for the ZICs, prepared by the (a) Ad-Free and (b) SY-containing (3 mM) electrolytes. (c) corresponding contribution ratios versus scanning rates calculated using Dunn's method for the Ad-Free electrolyte.

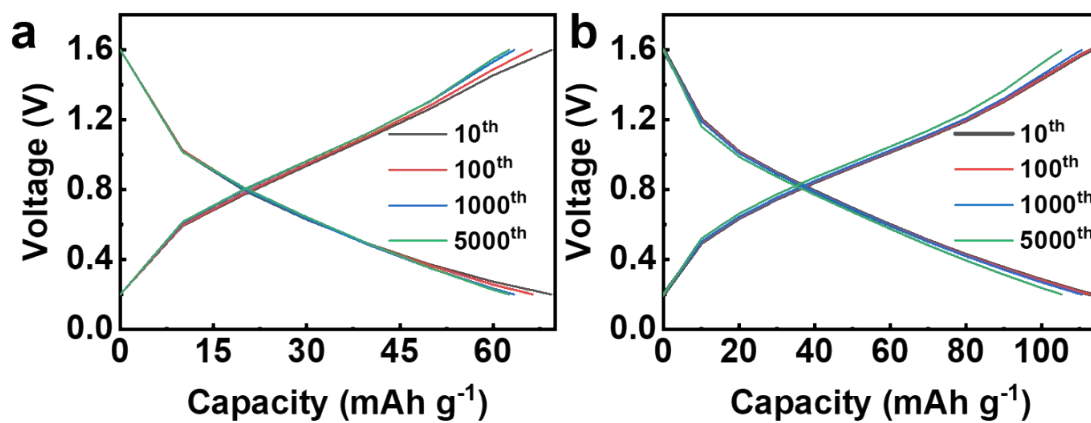


Figure S29 CD profiles obtained from the different cycles of the ZICs, prepared by the (a) Ad-Free and (b) SY-containing (3 mM) electrolytes.

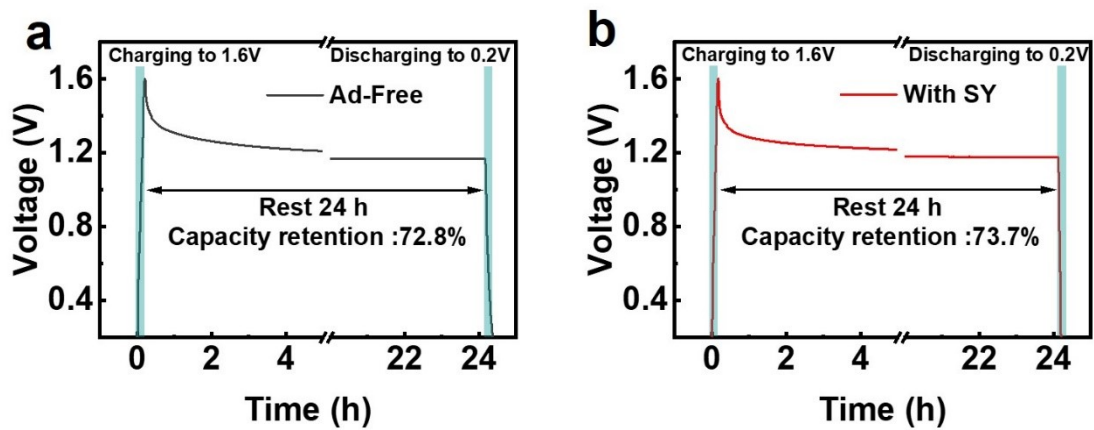


Figure S30 Evaluation of the self-discharge behavior of the ZICs, prepared by the (a) Ad-Free and (b) SY-containing (3 mM) electrolytes.

Supplementary Note 7: Versatility of Azobenzene Molecules

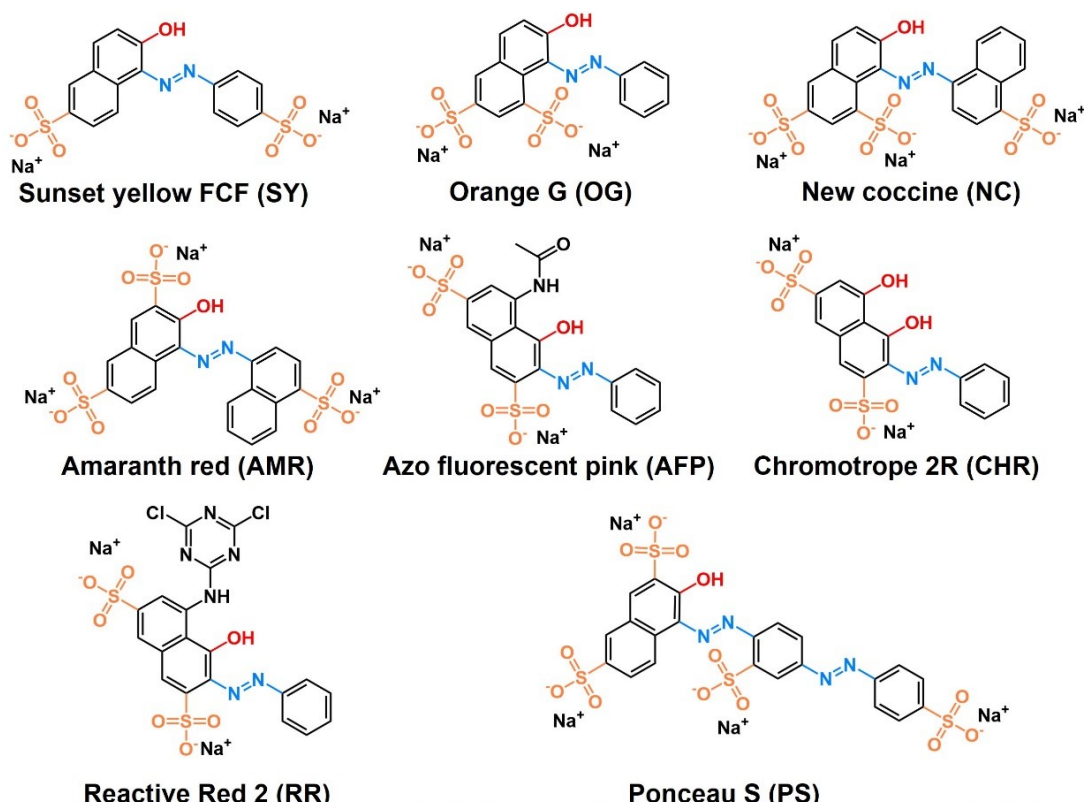


Figure S31 Chemical Structure of azobenzene compounds.

In exploring the versatility of azobenzene molecules, a series of derivatives were examined for fabrications of redox electrolytes. As shown in Figure S30, these compounds exhibit a diverse range of energy levels, which are influenced by the substituent modification with the azobenzene backbone. The visualizations of electron density distribution underscore how functional groups modulate the electron-rich regions associated with HOMO energy levels and the electron-poor regions linked to LUMO energy levels^{34, 35}. The results demonstrate that optimizing structural and molecular characteristics can tailor redox potential and enhance electrochemical stability.

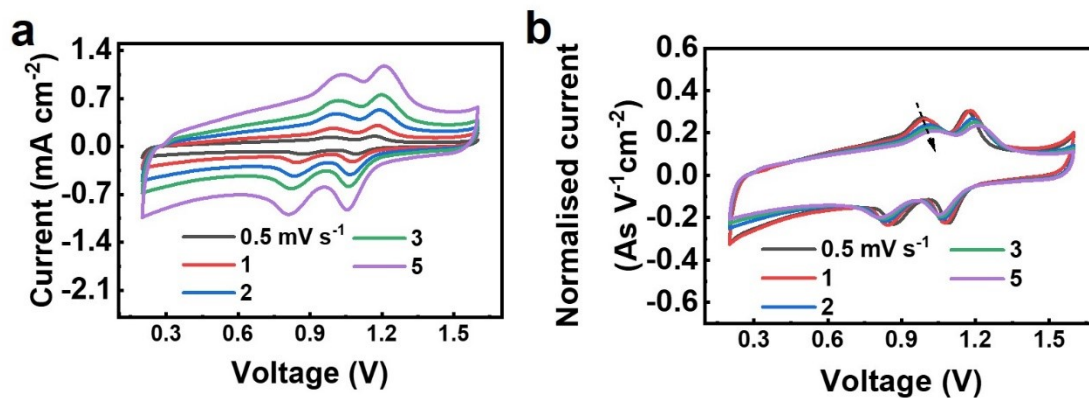


Figure S32 CV profiles of the ZIC prepared with the OG-containing electrolyte: a) at various scan rates and b) normalized by scan rates.

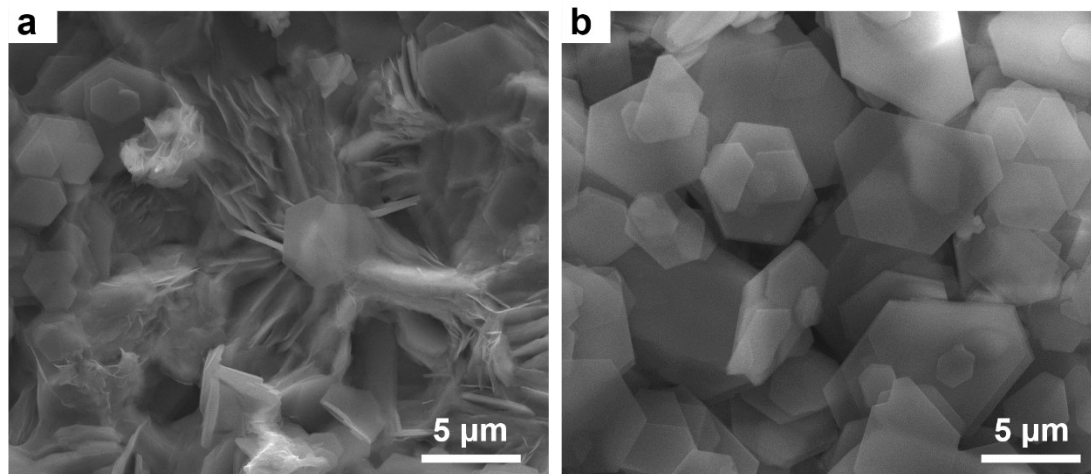


Figure S33 SEM images of Zn electrodes obtained from Zn//Zn cells at 2 mA cm^{-2} and 1 mAh cm^{-2} after 200 cycles, using the (a) Ad-Free and (b) OG-containing electrolytes.

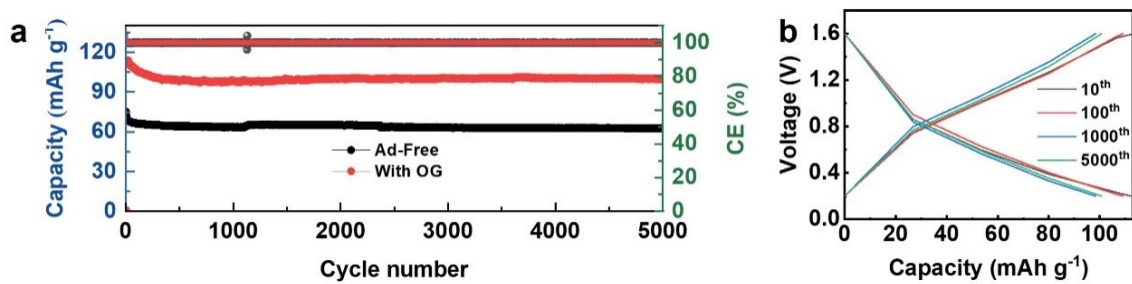


Figure S34 (a) Cycling performance at 0.6 A g⁻¹ of the ZICs, prepared by Ad-Free and OG-containing electrolytes. (b) CD profiles obtained from the different cycles of the ZICs, prepared by the OG-containing electrolytes.

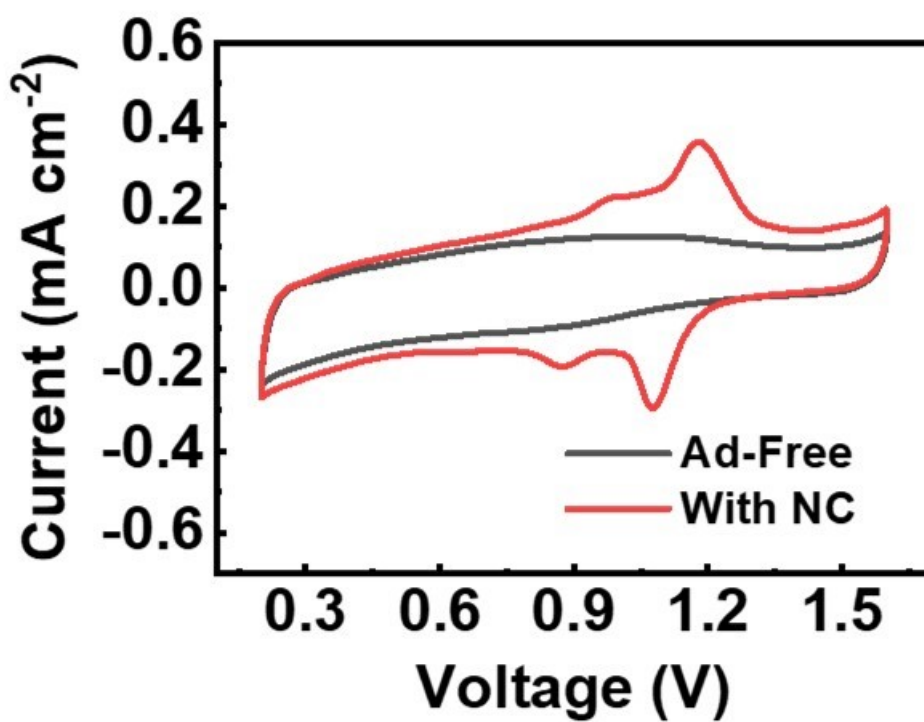
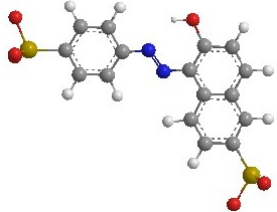
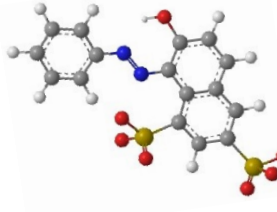
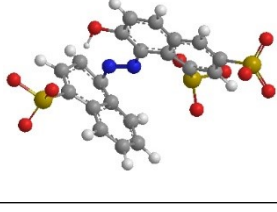
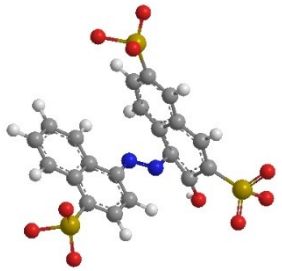
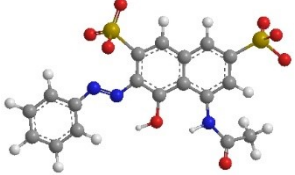
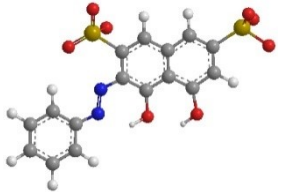
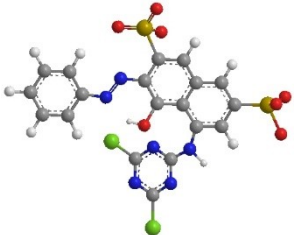
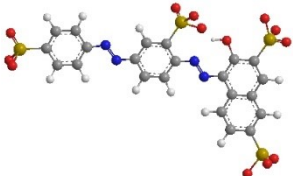


Figure S35 CV profiles at a scan rate of 1.0 mV s⁻¹ for the ZICs, prepared by the Ad-Free and NC-containing (3mM) electrolytes.

Table S4 3D chemical structure and physical-chemical properties of azobenzene molecules.

Name	Structural	Molecular weight (g mol ⁻¹)	Connolly accessible area ^{36, 37} (Å ²)	Connolly molecular area ^{36, 37} (Å ²)	Polar surface area ^{38, 39} (Å ²)	Connolly solvent excluded volume ^{36, 40} (Å ³)	Log P ⁴¹⁻⁴³ (hydrophobicity)	Length (Å)	Width (Å)	Depth (Å)	CAS
Sunset yellow FCF (SY)		452.37	563.903	304.594	159.35	256.215	2.25	17.398	10.357	5.620	2783-94-0
Orange G (OG)		452.37	535.758	293.48	159.35	257.903	2.25	15.689	10.023	5.746	1936-15-8
New coccine (NC)		604.46	618.725	354.718	216.55	343.556	2.16	15.258	9.417	8.785	2611-82-7

Amaranth red (AMR)		604.47	641.925	369.359	216.55	347.026	2.57	14.29 5	12.9 27	7.7 81	915- 67-3
Azo fluorescent pink (AFP)		509.41	581.108	315.423	188.45	269.334	1.49	16.88 0	11.7 95	5.8 69	3734 -67-6
Chromotrope 2R (CHR)		468.36	561.169	306.993	179.58	306.993	1.84	17.09 4	10.0 03	5.9 02	4197 -07-3
Reactive Red 2 (RR)		615.33	679.824	387.715	208.46	352.507	2.488	17.00 3	14.9 90	6.7 19	1780 4-49- 8

Ponceau S (PS)		760.57	811.996	459.211	298.47	401.013	2.05	22.21 0	13.3 78	5.9 52	6226 -79-5
----------------	---	--------	---------	---------	--------	---------	------	------------	------------	-----------	---------------

References

1. M. L. Connolly, *Journal of the American Chemical Society*, 1985, **107**, 1118-1124.
2. M. L. Connolly, *Journal of Molecular Graphics*, 1993, **11**, 139-141.
3. A. Leo, P. Y. C. Jow, C. Silipo and C. Hansch, *Journal of Medicinal Chemistry*, 1975, **18**, 865-868.
4. L. Zhang, C. Zhang and E. J. Berg, *Advanced materials*, 2024, DOI: 10.1002/adma.202407852, e2407852.
5. G. Ma, W. Yuan, X. Li, T. Bi, L. Niu, Y. Wang, M. Liu, Y. Wang, Z. Shen and N. Zhang, *Advanced materials*, 2024, DOI: 10.1002/adma.202408287.
6. Z. Cheng, K. Wang, J. Fu, F. Mo, P. Lu, J. Gao, D. Ho, B. Li and H. Hu, *Advanced Energy Materials*, 2024, DOI: 10.1002/aenm.202304003, 2304003.
7. C. Huang, J. Mao, S. Li, W. Zhang, X. Wang, Z. Shen, S. Zhang, J. Guo, Y. Xu, Y. Lu and J. Lu, *Advanced Functional Materials*, 2024, DOI: 10.1002/adfm.202315855, 2315855-2315862.
8. X. Wu, J. J. Hong, W. Shin, L. Ma, T. Liu, X. Bi, Y. Yuan, Y. Qi, T. W. Surta, W. Huang, J. Neufeind, T. Wu, P. A. Greaney, J. Lu and X. Ji, *Nature Energy*, 2019, **4**, 123-130.
9. L. Zheng, H. Li, X. Wang, Z. Chen, C. Hu, K. Wang, G. Guo, S. Passerini and H. Zhang, *ACS Energy Letters*, 2023, **8**, 2086-2096.
10. R. Wang, M. Yao, M. Yang, J. Zhu, J. Chen and Z. Niu, *Proceedings of the National Academy of Sciences of the United States of America*, 2023, **120**, e2221980120.
11. S. Roldan, C. Blanco, M. Granda, R. Menendez and R. Santamaria, *Angewandte Chemie*, 2011, **50**, 1699-1701.
12. D. Xi, A. M. Alfaraidi, J. Gao, T. Cochard, L. C. I. Faria, Z. Yang, T. Y. George, T. Wang, R. G. Gordon, R. Y. Liu and M. J. Aziz, *Nature Energy*, 2024, **9**, 479-490.
13. X. Zu, L. Zhang, Y. Qian, C. Zhang and G. Yu, *Angewandte Chemie*, 2020, **59**, 22163-22170.
14. T. Shimizu, N. Tanifuji and H. Yoshikawa, *Angewandte Chemie International Edition*, 2022, **61**, e202206093.
15. D. Vonlanthen, P. Lazarev, K. A. See, F. Wudl and A. J. Heeger, *Advanced materials*, 2014, **26**, 5095-5100.
16. M. Luo, X. Gan, C. Zhang, Y. Yang, W. Yue, I. Zhitomirsky and K. Shi, *Advanced Functional Materials*, 2023, **33**, 2305041.
17. M. P. Kamil, W. Al Zoubi, D. K. Yoon, H. W. Yang and Y. G. Ko, *Chem. Eng. J.*, 2020, **391**, 123614.
18. T. Hussain, M. Kaseem and Y. G. Ko, *Corros. Sci.*, 2020, **170**, 108663.
19. M. K. Awad, M. R. Mustafa and M. M. A. Elnga, *J. Mol. Struct.*, 2010, **959**, 66-74.
20. G. Gece, *Corros. Sci.*, 2008, **50**, 2981-2992.
21. D. Li, T. Sun, T. Ma, W. Zhang, Q. Sun, M. Cheng, Z. Zha, W. Xie and Z. Tao, *Advanced Functional Materials*, 2024, DOI: 10.1002/adfm.202405145.
22. E. Titov, *Physical Chemistry Chemical Physics*, 2022, **24**, 24002-24006.
23. T. Wei, L. e. Mo, Y. Ren, H. Zhang, M. Wang, Y. He, P. Tan, Z. Li, W. Chen and L. Hu, *Energy Storage Materials*, 2024, **70**.
24. K. Wang, T. Qiu, L. Lin, H. Zhan, X.-X. Liu and X. Sun, *Energy Storage Materials*, 2024, **70**,

103516.

25. C. Li, X. Zhang, G. Qu, S. Zhao, H. Qin, D. Li, N. Li, C. Wang and X. Xu, *Advanced Energy Materials*, 2024, DOI: 10.1002/aenm.202400872.
26. A. M. Khedr and M. Gaber, *Spectroscopy Letters*, 2005, **38**, 431-445.
27. I. Guezguez, A. Ayadi, K. Ordon, K. Iliopoulos, D. G. Branzea, A. Migalska-Zalas, M. Makowska-Janusik, A. El-Ghayoury and B. Sahraoui, *The Journal of Physical Chemistry C*, 2014, **118**, 7545-7553.
28. L. Ji, L. Peng, T. Chen, X. Li, X. Zhu and P. Hu, *Talanta Open*, 2022, **5**, 100084-100091.
29. M. A. I. Al-Gaber, H. M. Abd El-Lateef, M. M. Khalaf, S. Shaaban, M. Shawky, G. G. Mohamed, A. Abdou, M. Gouda and A. M. Abu-Dief, *Materials (Basel)*, 2023, **16**.
30. M. Orojloo, R. Arabahmadi, F. Naderi, F. Parchegani, M. Solimannejad, P. Zolgharnein and S. Amani, *Chemical Papers*, 2017, **72**, 719-729.
31. E. Y. Hashem, M. S. Saleh, N. O. A. Al-Salahi and A. K. Youssef, *Food Analytical Methods*, 2016, **10**, 865-875.
32. A. Steinegger, O. S. Wolfbeis and S. M. Borisov, *Chem Rev*, 2020, **120**, 12357-12489.
33. X. Luo, A. Zaitoon and L. T. Lim, *Compr Rev Food Sci Food Saf*, 2022, **21**, 2489-2519.
34. Y.-Y. Hsieh and H.-Y. Tuan, *Energy Storage Materials*, 2024, **68**.
35. Y. Liu, S. Yang, H. Guo, Z. Wang, J. Liu, N. Chen and X. Gong, *Energy Storage Materials*, 2024, **73**.
36. M. L. Connolly, *J. Mol. Graph. Model.*, 1993, **11**, 139-141.
37. M. L. Connolly, *Science* 1983, **221**, 709-713.
38. X. Y. Kong, Y. Ding, R. Yang and Z. L. Wang, *Science*, 2004, **303**, 1348-1351.
39. P. Ertl, B. Rohde and P. Selzer, *J. Med. Chem.*, 2000, **43**, 3714-3717.
40. M. L. Connolly, *J. Appl. Crystallogr.*, 1985, **18**, 499-505.
41. A. Leo, P. Y. Jow, C. Silipo and C. Hansch, *J. Med. Chem.*, 1975, **18**, 865-868.
42. T. Kim and S. Jeon, *Fibers Polym.*, 2013, **14**, 105-109.
43. X.-F. Tan, S.-S. Zhu, R.-P. Wang, Y.-D. Chen, P.-L. Show, F.-F. Zhang and S.-H. Ho, *Chin. Chem. Lett.*, 2021, **32**, 2939-2946.